PHYSICAL REVIEW B **110**, 064411 (2024)

Influence of the magnetic inertia on the self-oscillation in spin-orbit torque-driven tripartite antiferromagnets with a 120° rotation symmetry

Peng-Bin He[*]
School of Physics and Electronics, Hunan University, Changsha 410082, China

(Received 29 April 2024; revised 23 July 2024; accepted 26 July 2024; published 8 August 2024)

Tripartite antiferromagnets (AFMs) with a 120° spin order, exhibiting unconventional transport properties, facilitate detecting AFM states. This inspires some studies on terahertz self-oscillations in these spin structures. However, self-oscillations under the influence of magnetic inertia, which comes out in the ultrafast dynamics, have not yet been unveiled. Here, resorting to the symmetry and numeric results, an effective analytic theory, which allows for a detailed analytic treatment, is developed to describe the self-oscillation triggered by a spin-orbit torque. Then, the phase boundaries of self-oscillation are determined, and it is found that the magnetic inertia wipes out the upper threshold, extending the useful frequency range. Furthermore, the precession holds almost in-plane with increasing current, resulting in a large-amplitude steady oscillation. Finally, the effect of Dzyaloshinsky-Moriya interaction on the tunable range of self-oscillation is discussed briefly. In virtue of the wide frequency tunability granted by the inertia and the unique features of the tripartite AFMs, this study may provide a significant contribution to the spintronic terahertz applications.

DOI: 10.1103/PhysRevB.110.064411

I. INTRODUCTION

Coherent precession of magnetization driven by spin torques is a common dynamics in various magnets, from which the nano-oscillators of electromagnetic waves can be envisioned. In ferromagnets (FMs), the characteristic frequency of this precession is determined by the energy scales of the anisotropy or the applied field, having the order of a few gigahertz. By contrast, the precession in antiferromagnets (AFMs) is principally propelled by the strong intersublattice exchange interaction because of the relative tilting between the sublattice magnetic moments. In view of the energy scale of exchange interaction, the AFM precessional frequency is generally in the terahertz (THz) regime.

According to its dynamic feature, the precession of magnetization can be classified into linear and nonlinear types. In the linear regime, the magnetic moments precess around a well-defined equilibrium direction with a small cone angle, bringing about the small-amplitude magnetic oscillation. Usually, to keep a steady linear oscillation, a periodic stimulation is required. Under an increasing antidamping spin torque, which causes the amplitude of linear oscillation to grow exponentially, a self-oscillation emerges beyond the instability of linear modes. AFM self-oscillation is a periodic precession of magnetization triggered by the nonperiodic spin torques. It is the exchange field that drives this nonlinear oscillation in the promise of a balance between the antidamping spin torque and the intrinsic magnetic damping. For self-oscillation, the large amplitude owing to the large cone angle of precession leads to the large power. Therefore, AFM self-oscillation is not only a fundamental issue on the nonlinear magnetic dynamics but also practically important for THz applications.

At present, the studies on THz self-oscillation of magnetization have mostly focused on the collinear AFMs [1–9], whereas the self-oscillations of noncollinear AFMs are rarely investigated [10–13]; neither has the effect of magnetic inertia been involved. There are a kind of tripartite noncollinear AFMs, in which the neighboring spins in a triangular structure make a 120° angle. Such spin structure, existing in some antiperovskite and hexagonal manganese compounds, displays large anomalous Hall effects [14], by which different noncollinear configurations can be distinguished. Specially, the spin-torque-driven switching [15–18] and oscillation of the AFM order may induce changing of the anomalous Hall conductivity, and thus be detected by this effect. For these noncollinear AFMs, besides brief mentions of the magnetization oscillation in Refs. [15,18], the thresholds and frequencies of oscillation have been explored analytically [10]. Furthermore, Lund *et al.* [12] proved that a gapless self-oscillation can be achieved through changing the chirality of ground state by the Dzyaloshinskii-Moriya interaction (DMI). Hu *et al.* [13] emphasized the key role of magnetic anisotropy in the emerging of oscillating states. A detection scheme [11] was also proposed to extract the THz oscillations as time-varying voltage signals.

Although the few works above [10–13] demonstrate some fascinating properties of the self-oscillations in noncollinear AFMs, a major question is that there exists an upper limit of the frequency, restricting the available frequency range. To settle this matter, one can resort to the magnetic inertia [19], which may help in preserving the large-angle precession once it has begun. In the Landau-Lifshitz-Gilbert (LLG) phenomenology, the magnetic inertia is introduced as a higher-order term in the dynamic equation. The

---

[*] Contact author: hepengbin@hnu.edu.cn

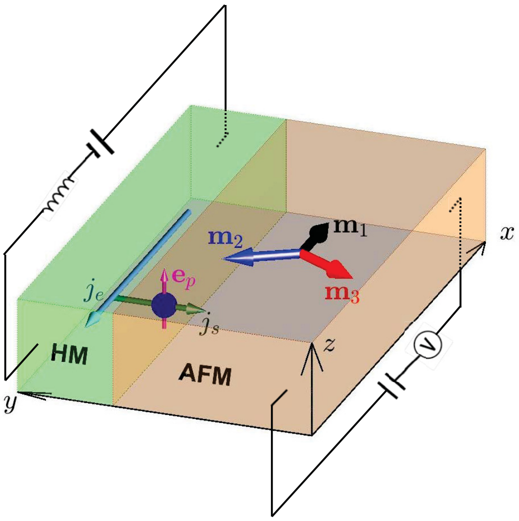

FIG. 1. A schematic of the heterostructure: A trisublattice AFM film is adjacent to a heavy metal layer. j_e and j_s are the electric and spin currents. $\mathbf{e}_p$ denotes the spin polarization.

inertial LLG equation can be derived from various theories or models, such as the classical mechanics [20–22], the nonequilibrium thermodynamics [23], the breathing Fermi surface model [24,25], the Dirac theory [26,27], the retardation effect [28], first principles [29], the Langevin equation [30], and the nonequilibrium Green's function [31]. Except these efforts on the mechanism of magnetic inertia, a few experiments [32–34] evidence the spin nutation, which is a typical inertial effect. Moreover, intensive theoretical research has been spurred on different inertial effects, such as the nutation resonances in FMs [35–42] and AFMs [43–45], the nutational auto-oscillation in FMs [46], the inertial spin waves [47–52], and the nutational switching [53–56].

In this work, the inertial self-oscillations triggered by a damping-like spin-orbit torque (SOT) will be investigated in the tripartite noncollinear AFMs with a 120° spin order, to describe which a minimal model is employed in the formalism of three interacting macrospins [57–61].

The paper is structured as follows. The model and method are introduced in Sec. II, supplemented with Appendix A. In Sec. III, the phase boundaries of self-oscillation are defined by the linear stability analysis and the energy-averaging technique, supplemented with Appendixes B, C, and D. The influence of inertia is also explored in term of the frequency and amplitude of self-oscillation. In Sec. IV, the role of DMI on the lower threshold is discussed. Finally, some discussions and summaries are presented in Secs. V and VI.

II. MODEL AND METHOD

The considered model is the tripartite AFM film with a 120° spin order adjacent to a current-driven heavy metal (HM) layer, as shown in Fig. 1. The AFM dynamics is modeled by three exchange-coupled inertial Landau-Lifshitz-Gilbert (LLG) equations including the SOTs [62],

$$\frac{d\mathbf{m}_i}{dt} = \mathbf{m}_i \times \frac{d\mathcal{E}}{d\mathbf{m}_i} + \alpha \mathbf{m}_i \times \frac{d\mathbf{m}_i}{dt} + \eta \mathbf{m}_i \times \frac{d^2\mathbf{m}_i}{dt^2} + \boldsymbol{\tau}_i, \quad (1)$$

where $\mathbf{m}_i$ is the unit vector of magnetization in three sublattices marked by $i = 1, 2, 3$. α is the Gilbert constant of damping. η is the inertial relaxation time ranging from fs to ps, as predicted in the *ab initio* calculation [63] and the nutation experiments [32–34].

Here, the inhomogeneous exchange contribution is ignored. So, one can focus on the coherent magnetic dynamics within the framework of a macrospin model, which is a reasonably good approximation for a small-size sample. Then, including the exchange interaction, the magnetocrystalline anisotropy, and the DMI, the magnetic energy reads [57–61],

$$\mathcal{E} = \omega_E \sum_{\langle ij \rangle} \mathbf{m}_i \cdot \mathbf{m}_j - \omega_A \sum_i \left(\mathbf{m}_i \cdot \mathbf{e}_A^i\right)^2 + \omega_D \sum_{\langle ij \rangle} \mathbf{e}_D \cdot (\mathbf{m}_i \times \mathbf{m}_j), \quad (2)$$

where the symbol $\langle ij \rangle$ indicates the sum over the pairs $(i, j) = (1, 2), (2, 3)$, and $(3, 1)$. $\mathbf{e}_D$ is the unit DM vector, assumed to lie normal to the film plane. $\mathbf{e}_A^i$ represents the unit vector along the easy axis of the ith sublattice, and is written as

$$\mathbf{e}_A^i = \cos\left[(i-1)\frac{2\pi}{3}\right]\mathbf{e}_x + \sin\left[(i-1)\frac{2\pi}{3}\right]\mathbf{e}_y. \quad (3)$$

All the terms in Eq. (2) have been rescaled to have the dimension of frequency. $\omega_E = \gamma_0 H_E$, $\omega_D = \gamma_0 H_D$, and $\omega_A = \gamma_0 H_A$, with H_E, H_D, and H_A being the effective fields due to the intersublattice exchange coupling, the DMI, and the anisotropy. $\gamma_0 = g\mu_0\mu_B/\hbar$ is the gyromagnetic ratio with g being the Landé g factor, μ_0 the vacuum susceptibility, μ_B the Bohr magneton, and $\hbar$ the reduced Plank constant.

In Eq. (2), the magnetic energy is defined on the one-layer lattice. In fact, the anisotropy might depend on the crystal plane. For example, in $\mathrm{Mn_3Sn}$ [60,61], the triangular spin structures form an ABAB stacking sequence. The directions of easy axes in the adjacent triangular structures are different. So, the complete magnetic energy should involve two triangular spin structures. However, in the SOT scheme considered (see Fig. 1), the spin polarization is perpendicular to the easy axes of both triangular structures which are parallel, resulting in similar dynamics driven by the SOT. Thus, this single-layer formalism, adopted in a large number of literature [57–61], can decipher the main features of magnetization dynamics. Furthermore, this minimal model enables an exhaustive analytic investigation.

The last term in Eq. (1) is the SOTs, generated by the spin transfer between the local magnetic moments and the spin currents produced in the HM layer. Including the damping-like and fieldlike terms, the SOTs are expressed as

$$\boldsymbol{\tau}_i = -\omega_T \mathbf{m}_i \times (\mathbf{m}_i \times \mathbf{e}_p) - \beta\omega_T (\mathbf{m}_i \times \mathbf{e}_p), \quad (4)$$

where $\mathbf{e}_p$ is the spin polarization along the film normal, as indicated in Fig. 1. β denotes the ratio of the fieldlike SOT to the damping-like one. In the unit of frequency, the strength of SOTs reads

$$\omega_T = \frac{\mu_B}{eM_s d}\xi j_e, \quad (5)$$

with d being the thickness of the AFM layer, e the element charge, M_s the sublattice saturation magnetization, and j_e the electric current density. ξ is the SOT efficiency which equals $T_{\mathrm{int}}\theta_{\mathrm{sh}}$ [64,65], with θ_{sh} being the spin Hall angle [62], and T_{int} the spin transparency [66] of the HM-AFM interface.

First of all, Eq. (1) is solved numerically by the solver ode45 of Matlab (see Appendix A for details). The arrays of components of $\mathbf{m}_1$, $\mathbf{m}_2$, and $\mathbf{m}_3$ are obtained at a time sequence for varying ω_T and η. From these data, the evolutions of $\mathbf{m}_1$, $\mathbf{m}_2$, and $\mathbf{m}_3$ are plotted directly, and the frequency and amplitude are also extracted indirectly.

The evolutions of $\mathbf{m}_1$, $\mathbf{m}_2$, and $\mathbf{m}_3$ (see, for examples, Fig. 5 in Appendix A) show that the AFM ground state evolves into a steady oscillation around the z axis with $\theta_1 = \theta_2 = \theta_3$ and $\phi_2 - \phi_1 = \phi_3 - \phi_2 = 2\pi/3$ for the righthanded ground state, and $-2\pi/3$ for the lefthanded one. Here, (θ_i, ϕ_i) are the polar and azimuthal angles, defined by $\mathbf{m}_i = (\sin\theta_i \cos\phi_i,\ \sin\theta_i \sin\phi_i,\ \cos\theta_i)$. Consequently, the magnetization dynamics is reduced to the rigid rotation of a spin frame with a definite precessional angle. Namely, the dynamics of self-oscillation is captured by the ansatz $\theta_1 = \theta_2 = \theta_3 = \theta$, as well as $\phi_1 = \phi(t)$, $\phi_2 = \phi(t) \pm 2\pi/3$, and $\phi_3 = \phi(t) \pm 4\pi/3$. Upon substitution into Eq. (1), and defining $\mathbf{n} = (\sin\theta\cos\phi,\ \sin\theta\sin\phi,\ \cos\theta)$, this ansatz results in the following effective equation of motion:

$$\frac{d\mathbf{n}}{dt} = \mathbf{n} \times \frac{d\mathcal{E}_n}{d\mathbf{n}} + \alpha\mathbf{n} \times \frac{d\mathbf{n}}{dt} + \eta\mathbf{n} \times \frac{d^2\mathbf{n}}{dt^2} + \boldsymbol{\tau}_n, \tag{6}$$

where the reduced magnetic energy reads

$$\mathcal{E}_n = \tfrac{1}{2}(3\omega_E - \sqrt{3}\omega_D)(\mathbf{n}\cdot\mathbf{e}_z)^2 - \omega_A(\mathbf{n}\cdot\mathbf{e}_x)^2, \tag{7}$$

and the effective SOTs are

$$\boldsymbol{\tau}_n = -\omega_T[\mathbf{n} \times (\mathbf{n} \times \mathbf{e}_z) + \beta\mathbf{n} \times \mathbf{e}_z]. \tag{8}$$

From Eq. (7), it can be seen that the equivalent system of $\mathbf{n}$ is a ferromagnet-like film with a hard axis normal to the film and an easy axis along the x direction. The easy-plane anisotropy arises from the intersublattice exchange and the DMI. The addition of DMI to the magnetic energy just gives rise to a redefinition of the exchange parameter ($\omega_E \rightarrow \omega_E - \sqrt{3}/3\omega_D$) for this single-vector equation. In general, $\omega_E \gg \omega_A$ or ω_D. So, this easy-plane anisotropy is much stronger than the easy-axis one.

Based on this reduced dynamic system governed by Eqs. (6)–(8), the phase boundaries of self-oscillation will be built by the stability analysis of equilibrium states and the averaging technique for the oscillation in the next section. For simplicity, the following discussions are limited to the case neglecting the field-like SOT.

III. PHASE DIAGRAM AND SELF-OSCILLATION

The phase boundaries of self-oscillation can be preliminarily defined by the stability analysis of equilibrium states. In the regions without stable equilibria, the self-oscillation happens possibly. This can be checked by solving Eq. (1) numerically. In addition, the thresholds of self-oscillation can be obtained by a method averaging the energy over precessional orbits, which has successfully been applied on the spin-torque-triggered self-oscillation in FM [67–70] and AFM [7,8,10]. Combining these analytic methods and the numeric calculations, a phase diagram will be constructed in the parameter plane spanned by the SOT strength ω_T and the inertial relaxation time η. Given the similar results for positive and negative ω_T, the discussions are restricted to positive ω_T hereafter.

A. Boundary between ferromagnetic state and self-oscillation

As demonstrated in a previous work [10], the FM states $\mathbf{m}_i = \pm\mathbf{e}_z$ (i.e., $\mathbf{n} = \pm\mathbf{e}_z$) are equilibria under a strong SOT. Here, for definition, $\mathbf{m}_i = \mathbf{e}_z$ is chosen, which may maintain for positive ω_T, as derived in Appendix B 2. Using linear stability analysis, it can be derived that (see Appendixes B 1 and B 2 for details of the derivation), in the experimentally reachable parameter regime, the stability conditions of FM state are $\eta < \eta_-$ and $\omega_T^- < \omega_T < \omega_T^+$, where

$$\eta_- = (1+\alpha^2)\frac{3\omega_E' + \omega_A}{2\omega_A^2}\left[1 - \sqrt{1 - \frac{1}{1+\alpha^2}\left(\frac{\omega_A}{3\omega_E' + \omega_A}\right)^2}\,\right], \tag{9}$$

and

$$\omega_T^{\pm} = \frac{\alpha}{2\eta}\left[1 \pm \sqrt{1 - 4\eta\left(3\omega_E' + \omega_A - \frac{\eta\omega_A^2}{1+\alpha^2}\right)}\,\right], \tag{10}$$

with $\omega_E' = \omega_E - \sqrt{3}/3\omega_D$.

B. Boundary between tilted antiferromagnetic state and self-oscillation

In the ground state without SOT, $\mathbf{m}_1$, $\mathbf{m}_2$, and $\mathbf{m}_3$ prefer to lie up along each easy axis, forming two degenerate 120° configuration (see the panel denoted by AFM in Fig. 2). The SOT tilts $\mathbf{m}_1$, $\mathbf{m}_2$, and $\mathbf{m}_3$ away from each easy axis, but remains in the 120° configuration, as schematically shown in the panel denoted by tilted AFM in Fig. 2. As demonstrated in Appendix C 1, these two tilted AFM states are formulated as

$$\mathbf{m}_i = \cos(\phi_0 - \Phi_i)\mathbf{e}_x + \sin(\phi_0 - \Phi_i)\mathbf{e}_y, \tag{11}$$

where $\Phi_i = (i-1)3\pi/2$, and the tilted angle reads

$$\phi_0 = -\frac{1}{2}\arcsin\frac{\omega_T}{\omega_A} \text{ or } \pi - \frac{1}{2}\arcsin\frac{\omega_T}{\omega_A}. \tag{12}$$

From Eq. (12), one can see that these solutions exist stably when $|\omega_T| < \omega_A$ (see details in Appendix C 2). However, the evolutions of $\mathbf{m}_1$, $\mathbf{m}_2$, and $\mathbf{m}_3$ indicate that the tilted AFM state becomes unstable not at $\omega_T = \omega_A$. As shown in Figs. 5(a) and 5(b), the instability occurs at $\omega_T = 0.210$ THz, which is obviously less than ω_A (0.258 THz). This means that the linear stability analysis is incapable of defining the instability of tilted AFM states.

To solve this question, it is convenient to resort to the averaging technique [67–69], by which, one can derive analytic expressions for the current that generates and sustains self-oscillations through averaging the energy over precessional orbits under the assumption of the weak damping and SOT. Additionally, this method can be utilized to calculate the lower threshold of self-oscillation [8,10,70]. By this method, the

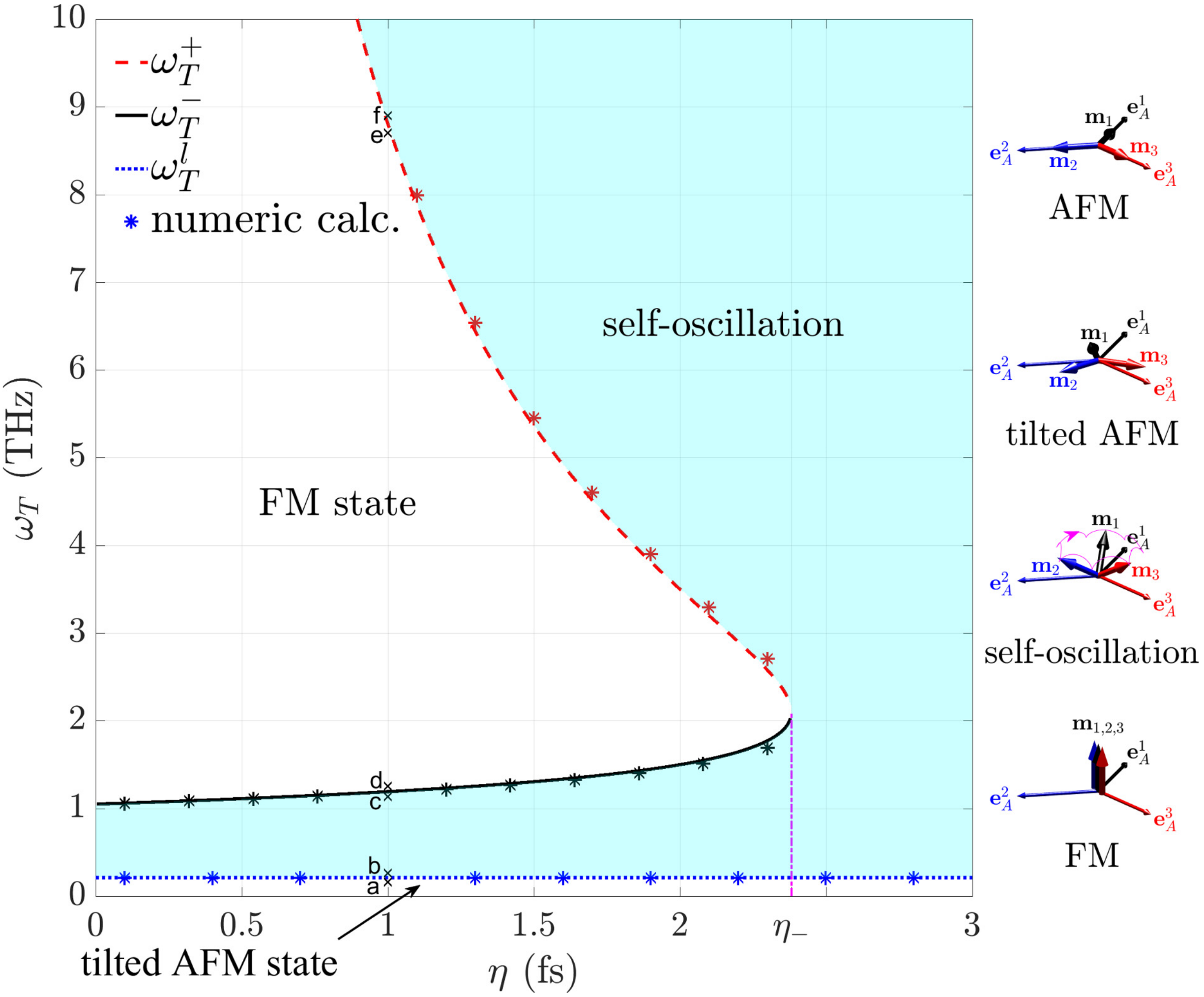

FIG. 2. Phase diagram in the parameter plane controlled by the SOT strength ω_T and the inertial relaxation time η. The boundaries are plotted according to Eqs. (10) and (13). The parameters used are $\alpha = 0.01$, $\omega_E = 34.9$ THz, and $\omega_A = 0.258$ THz, derived from the magnetic parameters of Mn$_3$Sn described in Ref. [60]. The DMI strength is taken as $\omega_D = 0.059$ THz, smaller than $\omega_A/(2\sqrt{3})$. These parameters are adopted for all figures throughout this paper unless specified otherwise. The markings of a, b, c, d, e, and f are picked up to see the evolutions of $\mathbf{m}_1$, $\mathbf{m}_2$, and $\mathbf{m}_3$ in Fig. 5 of Appendix A. Four states are depicted schematically in the right, where $\mathbf{e}_A^1$, $\mathbf{e}_A^2$, and $\mathbf{e}_A^3$ denote the easy axes of three sublattices.

lower threshold of self-oscillation is derived in Appendix D, which reads

$$\omega_T^l = \frac{2}{\pi}\sqrt{\frac{3\omega_E' + 2\omega_A}{3\omega_E'}}\left(\omega_A + \sqrt{6}\alpha\sqrt{\omega_A\omega_E'}\right). \qquad (13)$$

In the calculation of Eq. (13), the inertial term is ignored, which brings about the nutation on top of the precession. Although some closed-form analytic solutions have been derived for nutation of magnetization [40], it is particularly challenging to accomplish the curvilinear integral in Eq. (D3). Nevertheless, the inertial term is proportional to the square of frequency, and is relatively small at the lower threshold of self-oscillation due to the lower frequency. Therefore, a significant albeit approximate analytic formula [Eq. (13)] is achieved. Moreover, it can be found that Eq. (13) agrees well with the numeric results for small η [see the dotted line in Fig. 2 and the insets in Figs. 3(a) and 3(b)], and is slightly larger than the numeric values for larger η, as indicated in the insets of Figs. 3(c) and 3(d).

C. Influence of inertia

To corroborate above analytic results and illustrate the influence of inertia, Eqs. (10) and (13) are plotted in Fig. 2, in which the tilted AFM state, the self-oscillation, and the FM state can be discerned in the η-ω_T control plane. The numeric results are also shown for the phase boundaries, verifying the analytic predictions with good agreement. To test the behaviors of the three phases, several sets of parameters are picked up near the phase boundaries, as marked by the crosses in Fig. 2. The corresponding evolutions of $\mathbf{m}_1$, $\mathbf{m}_2$, and $\mathbf{m}_3$ are plotted in Fig. 5 of Appendix A. These exemplary plots confirm the division of phase regions.

Inspection of Fig. 2 reveals that there exist three distinct dynamic regimes with varying η. In the absence of inertia ($\eta = 0$), the tilted AFM state becomes unstable with ω_T

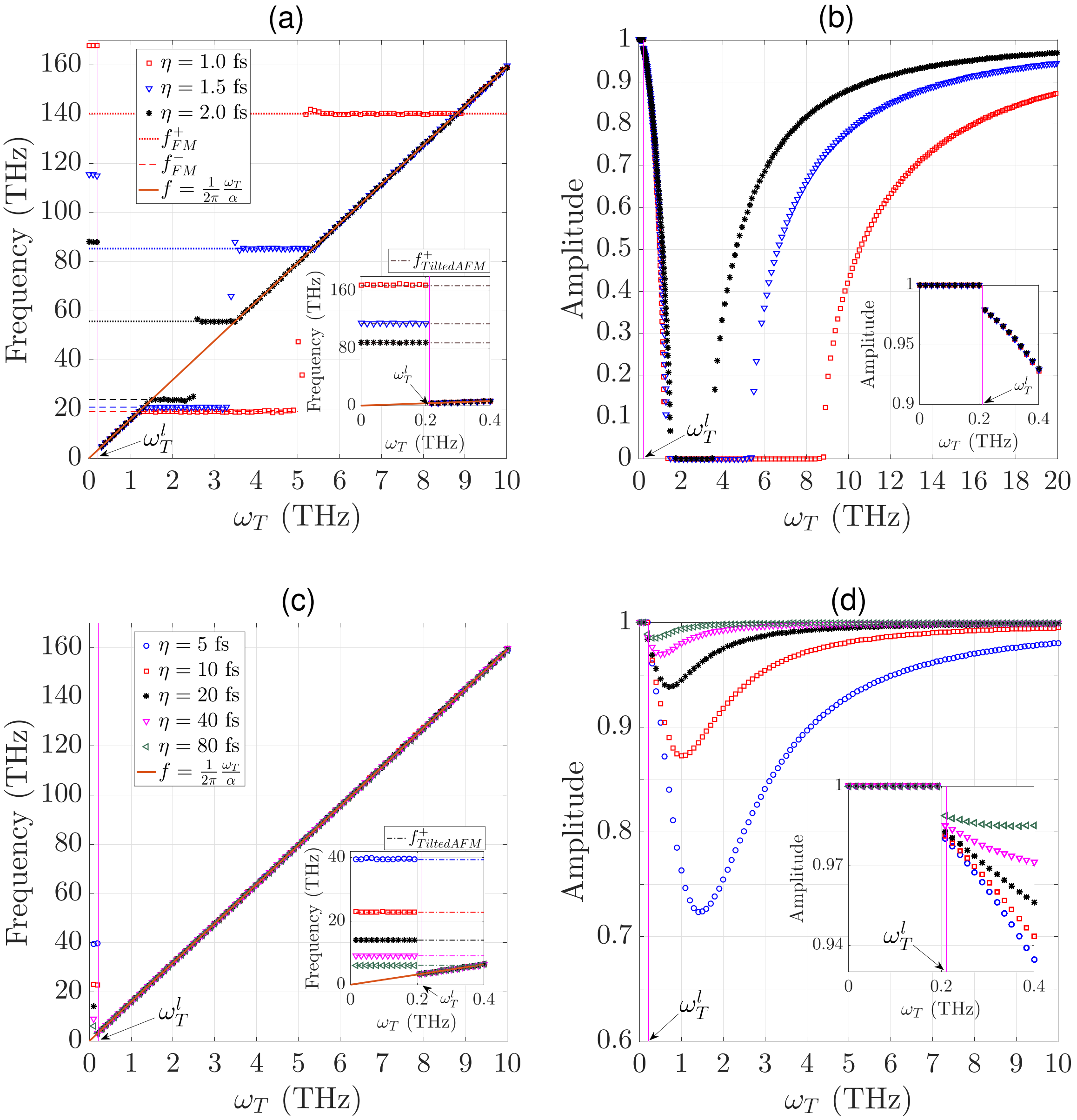

FIG. 3. The (a), (c) frequencies and (b), (d) amplitudes of self-oscillations as functions of the SOT strength ω_T for different inertial relaxation time η. The upper panels (a) and (b) correspond to the case $\eta < \eta_-$, and the lower panels (c) and (d) correspond to $\eta > \eta_-$. The insets show the magnified views around the lower threshold ω_T^l of self-oscillation. In the insets of (a) and (b), ω_T^l agrees well with the numeric results. In the insets of (c) and (d), ω_T^l is slightly larger than the numeric values. Markers are numeric results and lines are analytic expressions.

beyond ω_T^l. When $\omega_T^l < \omega_T < \omega_T^-$, the system enters the self-oscillation state (see the panel denoted by self-oscillation in Fig. 2). When $\omega_T > \omega_T^-$, the FM state (see the panel denoted by FM in Fig. 2) always exists. Note that ω_T^+ approaches infinity when $\eta = 0$. Here, the upper threshold of self-oscillations limits a useful frequency range. This case is a recurrence of the result in Ref. [10]. For weak inertia ($0 < \eta < \eta_-$), the tilted AFM state, the self-oscillation, and the FM state emerge in turn with increasing ω_T, similar to the case $\eta = 0$. However, the self-oscillation revives after $\omega_T > \omega_T^+$. It is noteworthy that the region of FM state shrinks with η increasing and disappears at $\eta = \eta_-$. When $\eta > \eta_-$, the self-oscillation always exists after the instability of tilted AFM state ($\omega_T > \omega_T^l$). These arguments indicate that the inertia expands the range of self-oscillation. Especially, there is no upper threshold of ω_T for slightly large η, in sharp contrast with the case without the magnetic inertia.

It should be noted that a small inertial relaxation time ($\eta_- \approx 2.4$ fs) dramatically changes the dynamic feature of AFMs driven by the SOT. This is not surprising if considering the ultrafast dynamics of AFM and the dependance of the magnetic inertia on the frequency. The inertial term in Eq. (1) involves the second-order derivative of $\mathbf{m}_i$. So, the inertial torque ($\propto \eta\omega^2$) strongly depends on the characteristic frequency of the magnetic dynamics. Given the very high frequencies of antiferromagnetic precession, it can be justified that the inertial effect in AFMs is remarkable even for small η. Recently, several theoretic works [43,45] also reported that the magnetic inertia with such small η ($\approx$1 fs) results in the nutation resonance.

D. Frequency and amplitude

Figure 3 shows the dependencies of the frequency and amplitude on ω_T. The amplitude is represented by the in-plane component of $\mathbf{m}_i$, i.e., $(1-m_{iz}^2)^{1/2}$, which is almost identical for the three sublattices and positively associated with the precessional angle.

Below ω_T^l, the frequency displayed in the insets of Figs. 3(a) and 3(c) belongs to the nutational oscillation on top of the tilted AFM state. In the leading order, the frequencies are analytically written as (see details in Appendix C 3)

$$f_{\text{AFM}}^{\pm}=\frac{\sqrt{1+\eta\widetilde{\omega}_E\pm\sqrt{(1+\eta\widetilde{\omega}_E)^2-8\eta^2\widetilde{\omega}_A\widetilde{\omega}_E}}}{2\sqrt{2}\pi\eta},\tag{14}$$

where $\widetilde{\omega}_E=3\omega_E'+\omega_A+3\widetilde{\omega}_A$, with $\widetilde{\omega}_A=(\omega_A^2-\omega_T^2)^{1/2}$. For $\eta=0$, f_{AFM}^{+} is infinity and the nutation no longer exists. Meanwhile, f_{AFM}^{-} becomes $[2\widetilde{\omega}_A(3\omega_E'+\omega_A+\widetilde{\omega}_A)]^{1/2}$, which is just the precessional resonance frequency without inertia. The amplitude of linear mode is small and not shown here. The numeric calculations [the insets of Figs. 3(b) and 3(d)] exhibit the value of $(1-m_{iz}^2)^{1/2}\approx 1$ for tilted AFM states. In this region ($\omega_T<\omega_T^l$), the results are qualitatively identical for varying η. However, for $\omega_T>\omega_T^l$ the scenarios are different for $\eta<\eta_-$ and $\eta>\eta_-$, which must be considered separately.

First, for $\eta<\eta_-$, the self-oscillation breaks off with ω_T between ω_T^- and ω_T^+, and the FM state arises instead, as illustrated in Figs. 2, 3(a), and 3(b). So, in this interval, the plotted frequencies belong to the linear modes around FM states, which reads (see details in Appendix B 3),

$$f_{FM}^{\pm}=\frac{\sqrt{1-2\eta\omega_A-6\eta\omega_E'\pm\sqrt{(1-2\eta\omega_A)^2-12\eta\omega_E'}}}{2\sqrt{2}\pi\eta}.\tag{15}$$

In the limit of $\eta\to 0$, f_{FM}^{+} approaches infinity, meaning the inertial mode dies away. At the same time, f_{FM}^{-} approaches $[3\omega_E'(2\omega_A+3\omega_E')]^{1/2}$, which is just the precessional resonance frequency without inertia. In Fig. 3(a), one can observe that a good agreement between the numerical simulation and the analytic formulaes is obtained for the frequencies of linear modes. When increasing ω_T, at $\omega_T=\alpha/(2\eta)$ [also marked by the circles in Figs. 6(a)–6(c)], there exists a jump from f_{FM}^{-} to f_{FM}^{+} according to the numeric results. The reason maybe lies in that the attenuation of precession is slower than nutation for $\omega_T<\alpha/(2\eta)$ but faster for $\omega_T>\alpha/(2\eta)$, as shown in Figs. 6(a)–6(c). To promote the accuracy of numeric calculation, it needs a steady oscillation after a long-time evolution. So, the data of slow-decay oscillation are adopted to calculate the frequency. This leads to the jump of dispersion in virtue of inversely changing of χ (attenuation factor) for precessional and nutational modes [see Figs. 6(a)–6(c)].

In the self-oscillation regions ($\omega_T^l<\omega_T<\omega_T^-$ and $\omega_T>\omega_T^+$), the frequency increases with ω_T almost linearly according to a universal leading-order formula for AFM self-oscillations,

$$f=\frac{1}{2\pi}\frac{\omega_T}{\alpha}.\tag{16}$$

Equation (16) can be derived from the reduced dynamic equation (6) by omitting ω_A. This approximation is reasonable because $\omega_E\gg\omega_A$. Equation (16) well reproduces the values of frequencies estimated from the numerical simulation, as shown in Fig. 3(a). In fact, different forms of Eq. (16) have been obtained by various methods for bipartite [1,3–7,9,10] and noncollinear AFMs [11–13].

As displayed in Fig. 3(b), in the interval $\omega_T^l<\omega_T<\omega_T^-$, the amplitude decreases with ω_T, and so does the precessional angle. At ω_T^-, the precessional angle vanishes and the self-oscillation ceases. All $\mathbf{m}_i$ keep along the z direction until $\omega_T>\omega_T^+$. In this interval ($\omega_T^-<\omega_T<\omega_T^+$), the system is in the FM state. The in-plane component of $\mathbf{m}_i$ is zero. Here, the amplitude of linear mode is too small to be shown. Beyond ω_T^+, the precessional cone reopens with an increasing cone angle. The amplitude increases quickly and nearly saturates to the maximum for large ω_T. In this case, $\mathbf{m}_i$ rotates almost in the x-y plane.

Second, for $\eta>\eta_-$, the FM state no longer appears, as illustrated in Figs. 2, 3(c), and 3(d). With ω_T beyond ω_T^l, the self-oscillation always exists, with its frequency continuously increasing with ω_T as Eq. (16). After a quick decrease, the amplitude increases gradually, then approaches a saturation for larger ω_T.

Finally, the influence of inertia on the frequency and amplitude is briefly discussed. Comparing the f-ω_T relations for different η shown in Figs. 3(a) and 3(c), it can be found that, although the inertia cannot affect the dependence of the frequency on the SOT strength, it expand the range of self-oscillation greatly. In theory, the frequency increases with the current without an upper limit, facilitating a wide-range linear control of the THz oscillator. With η increasing, the range of FM state is shrunk and disappears when $\eta>\eta_-$. Additionally, Figs. 3(b) and 3(d) reveal that, for larger η, the amplitude increases more easily with ω_T increasing, suggesting that the inertia favors an in-plane precession.

IV. EFFECT OF DZYALOSHINSKII-MORIYA INTERACTION

The DMI considerably affects the static configuration in the absence of SOT. In the magnetic energy [Eq. (2)], the anisotropy and DMI energies are overwhelmed by the exchange energy, which results in an in-plane 120° configuration, achieving a minimal exchange energy $-3\omega_E/2$. Specifically, $\mathbf{m}_1$, $\mathbf{m}_2$, and $\mathbf{m}_3$ lie in the x-y plane and are at an angle of 120° with respect to each other. Only considering the exchange energy, there are two kinds of degenerate configurations: $\mathbf{m}_1$, $\mathbf{m}_2$, and $\mathbf{m}_3$ rotate in the righthanded or lefthanded direction. Namely, $\phi_2-\phi_1=\phi_3-\phi_2=\pm120^\circ$, with ϕ_i being the angle between $\mathbf{m}_i$ and the positive x direction. Including the anisotropy energy, the degeneracy is lifted. For the righthanded configuration with a lowest energy $-3\omega_A$, $\mathbf{m}_i$ is aligned along the easy axis $\mathbf{e}_A^i$, i.e., $(\phi_1,\phi_2,\phi_3)=(0,120^\circ,240^\circ)$ or $(180^\circ,300^\circ,60^\circ)$, with the angle taking the remainder divided by 360. For the lefthanded configuration, the anisotropy energy is $-3\omega_A/2$ for arbitrary rotation of the 120° structure. By the principle of minimal energy, the righthanded configuration with $\mathbf{m}_i$ along each easy axis is the ground state when involving the exchange and anisotropy. If taking the DMI into account, the case becomes more interesting. The DMI energy is $(3\sqrt{3}/2)\omega_D$ for any righthanded configurations, and $-(3\sqrt{3}/2)\omega_D$ for lefthanded ones. From above analysis, the total energy of righthanded configuration is

$$E_R = -\tfrac{3}{2}\omega_E - 3\omega_A + \tfrac{3}{2}\sqrt{3}\omega_D, \tag{17}$$

while, the energy of lefthanded configuration is

$$E_L = -\tfrac{3}{2}\omega_E - \tfrac{3}{2}\omega_A - \tfrac{3}{2}\sqrt{3}\omega_D. \tag{18}$$

Comparing E_R with E_L, it can be inferred that the double-degenerate righthanded configuration is preferred energetically for $\omega_D < \omega_A/(2\sqrt{3})$. On the other hand, the infinitely degenerate lefthanded configuration [71] is favored for $\omega_D > \omega_A/(2\sqrt{3})$.

In the effective theory described by Eqs. (6)–(8), the DMI just redefines the exchange energy. In view of $\omega_E \gg \omega_D$, the DMI plays a minimal role for the properties of self-oscillations. However, the DMI determines the static configuration without a SOT, influencing the lower threshold of self-oscillations. Above discussions focus on the region $\omega_D < \omega_A/(2\sqrt{3})$, in which $\mathbf{m}_1$, $\mathbf{m}_2$, and $\mathbf{m}_3$ possess definite directions statically. When applying the current, to pull $\mathbf{m}_i$ from a definite direction to a precession, the SOT must overcome a barrier, resulting in a finite lower threshold [Eq. (13)]. In contrast, if $\omega_D > \omega_A/(2\sqrt{3})$, the static configuration is infinitely degenerate, so that the 120° lefthanded structure rotates freely in the x-y plane in spite of the anisotropy of each sublattice. Therefore, a tiny current can trigger a self-oscillation, meaning a zero lower threshold. This result can be verified by checking the evolutions of $\mathbf{m}_i$. In Ref. [12], this static configuration is referred to as the gapless phase. Here, a more detailed illustration is given from the standpoint of the static energetics and degeneracy.

V. DISCUSSION

First, to provide an intuitive picture of the self-oscillation, several dominating torques are schematically depicted on a unit magnetic sphere, as shown in Fig. 4. Generally, the magnetic inertia prompts fast nutational oscillations superimposed on the relatively slow precession. A lot of studies have been performed for the nutation in the linear regime [35–45]. In the nonlinear regime, the sum of two exchange torques exerted on $\mathbf{m}_i$ propels a lefthanded rotation, for which the damping torque drags $\mathbf{m}_i$ tilting away from the precessional axis. For a steady large-angle precession, the damping torque is canceled by the damping-like SOT. In a previous work [9] on a uniaxial collinear AFM, the purely time harmonic self-oscillation is produced in virtue of the rotation symmetry of the magnetic structure and the SOT scheme. This results in that the inertial torque is along the tangential direction of the orbit traced by the tip of $\mathbf{m}_i$. So, it only propels the precession and no nutation occurs. Here, due to the small in-plane anisotropy, the precessional orbit slightly deviates from the circle around the spin polarization. Thus, the inertial torque deviates from the tangential of orbit, but still lies in the tangent plane of sphere because it is perpendicular to $\mathbf{m}_i$. The tangential component of the inertial torque impels the precession, just like the exchange torque. Meanwhile, the perpendicular component forces $\mathbf{m}_i$ nodding up and down, generating a nutation on top of a large-angle precession, similar to the picture displayed in Fig. 1 of Ref. [19]. It is the tangential component of the inertial torque strengthens the driving torque of precession, postponing even erasing the upper limit of self-oscillation.

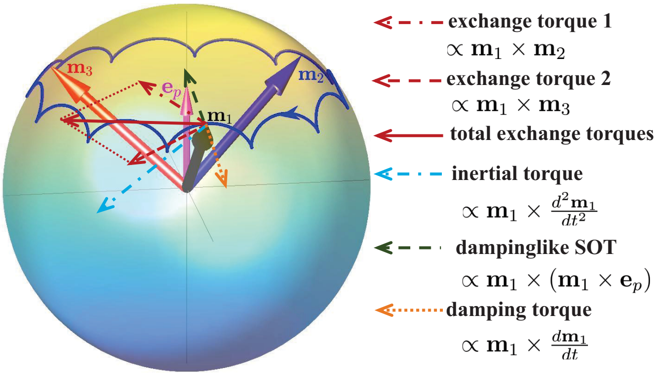

FIG. 4. Schematic view of the main torques born by $\mathbf{m}_1$. The same features persist for $\mathbf{m}_2$ and $\mathbf{m}_3$. The parameters chosen in the plot do not exactly represent a real system, just for demonstration purposes.

Second, the fieldlike SOT is not included in above calculations. Like a variable magnetic field, the fieldlike SOT modifies the precessional orbit and shifts the frequency of self-oscillation. However, it does not compete with the Gilbert damping and thus does not trigger a self-oscillation. For the tilted AFM state, the fieldlike SOT pulls $\mathbf{m}_i$ up from the film plane with a small angle owing to the strong exchange coupling. It modifies the thresholds and the frequency by a factor $1 + \alpha\beta$, analogous to the results taking no account of the magnetic inertia [10]. In general, $\alpha\beta \ll 1$, resulting in very small influences. Therefore, the fieldlike SOT only slightly affects the calculations quantitatively, but makes the analytic formulas complex. It is reasonable to ignore the fieldlike SOT from the qualitative point of view.

Finally, to ease the analytic description, the SOT strength is scaled into the frequency dimension, defined by Eq. (5). Then, the corresponding current density can be calculated by $j_e = 1/(T_{\mathrm{int}}\theta_{\mathrm{sh}})(eM_s d/\mu_B)\omega_T$. It follows that, a thinner AFM layer and/or a heavy metal with larger spin Hall angle will scale down the required current density for self-oscillations. In addition, choosing the materials with lower saturation magnetization and improving the interface spin transparency also favor decreasing the current.

VI. SUMMARY

In this paper, the role of magnetic inertia is explored on the self-oscillations triggered by the damping-like SOT in the thin AFM films with a 120° spin order. Motivated by the numeric simulation and enforced by the symmetry-allowed relations among $\mathbf{m}_1$, $\mathbf{m}_2$, and $\mathbf{m}_3$, the coupled magnetic dynamics of three sublattices is mapped onto a single-vector equation with biaxial anisotropy. The main advantage of this effective theory is its considerable simplicity compared with the three exchange-coupled LLG equations. Specifically, it allows for a detailed analytic treatment, which highlights the key physical features of self-oscillation.

By comparing the self-oscillations with and without a magnetic inertia in terms of the thresholds, frequencies and amplitudes, it is shown that the simulation and analytics of the inertial LLG equation predict a wider frequency window of self-oscillation than the LLG one. For relatively large inertial relaxation time, the frequency of self-oscillation can be continuously linearly adjusted by the current beyond the instability of AFM state, meanwhile, maintaining a large amplitude. In addition, relatively large DMI also enlarges the tunable range of self-oscillation by removing the lower threshold. Combining the favorable tunability endowed by the magnetic inertia and the unique transport features of 120°-order tripartite AFMs, these results may open new opportunities for the development of THz theory and technique.

ACKNOWLEDGMENTS

This work was supported by the NSF of Changsha City (Grant No. kq2208008) and the NSF of Hunan Province (Grant No. 2023JJ30116).

APPENDIX A: EVOLUTIONS OF $\mathbf{m}_1$, $\mathbf{m}_2$, AND $\mathbf{m}_3$

In this Appendix, the evolutions of $\mathbf{m}_1$, $\mathbf{m}_2$, and $\mathbf{m}_3$ are calculated and visualized for different parameters, which can not only verify the phase boundary obtained by the analytic calculations but also justify the effective model presented in Sec. II. In view of the unit-sphere constraint $|\mathbf{m}_i| = 1$, it is convenient to describe $\mathbf{m}_i$ by means of spherical coordinates θ_i and ϕ_i, defined by $\mathbf{m}_i = (\sin\theta_i\cos\phi_i,\ \sin\theta_i\sin\phi_i,\ \cos\theta_i)$. First the vectorial LLG equation (1) is written in terms of θ_i and ϕ_i by utilizing the time derivatives of $\mathbf{m}_i$ in spherical coordinates,

$$\frac{d\mathbf{m}_i}{dt} = \frac{d\theta_i}{dt}\mathbf{e}_i^{\theta} + \frac{d\phi_i}{dt}\sin\theta_i\mathbf{e}_i^{\phi}, \tag{A1}$$

$$\begin{aligned}\frac{d^2\mathbf{m}_i}{dt^2} = &-\left[\left(\frac{d\theta_i}{dt}\right)^2 + \left(\frac{d\phi_i}{dt}\right)^2\sin^2\theta_i\right]\mathbf{e}_i^r \\ &+\left[\frac{d^2\theta_i}{dt^2} - \left(\frac{d\phi_i}{dt}\right)^2\sin\theta_i\cos\theta_i\right]\mathbf{e}_i^{\theta} \\ &+\left(\frac{d^2\phi_i}{dt^2}\sin\theta_i + 2\frac{d\theta_i}{dt}\frac{d\phi_i}{dt}\cos\theta_i\right)\mathbf{e}_i^{\phi},\end{aligned} \tag{A2}$$

where $\{\mathbf{e}_i^r, \mathbf{e}_i^{\theta}, \mathbf{e}_i^{\phi}\}$ form the local spherical coordinate systems associated with $\mathbf{m}_i$, with $\mathbf{e}_i^r$ aligned with $\mathbf{m}_i$ and $\mathbf{e}_i^{\theta(\phi)}$ pointing in the direction of increasing θ_i (ϕ_i). Because of the inertial term, the LLG equation (1) are second-order differential equation. Then, in terms of the variables θ_i, ϕ_i, $d\theta_i/dt$ (Ω_i^{θ}), and $d\phi_i/dt$ (Ω_i^{ϕ}), Eq. (1) can be further converted into a system of first-order differential equations as follows:

$$\frac{d\theta_i}{dt} = \Omega_i^{\theta}, \tag{A3}$$

$$\frac{d\phi_i}{dt} = \Omega_i^{\phi}, \tag{A4}$$

$$\begin{aligned}\frac{d\Omega_i^{\theta}}{dt} = \frac{1}{\eta}\big\{&-\alpha\Omega_i^{\theta} + \Omega_i^{\phi}\sin\theta_i + \eta\big(\Omega_i^{\phi}\big)^2\sin\theta_i\cos\theta_i \\ &+\omega_E\sin\theta_i(\cos\theta_j + \cos\theta_k) \\ &-\omega_E\cos\theta_i[\sin\theta_j\cos(\phi_i - \phi_j) + \sin\theta_k\cos(\phi_i - \phi_k)] \\ &+\omega_D\cos\theta_i[\sin\theta_j\sin(\phi_i - \phi_j) - \sin\theta_k\sin(\phi_i - \phi_k)] \\ &+\omega_A\sin 2\theta_i\cos^2(\phi_i - \Phi_i)\big\},\end{aligned} \tag{A5}$$

$$\begin{aligned}\frac{d\Omega_i^{\phi}}{dt} = \frac{1}{\eta\sin\theta_i}\big\{&-\Omega_i^{\theta} - \alpha\Omega_i^{\phi}\sin\theta_i - 2\eta\Omega_i^{\theta}\Omega_i^{\phi}\cos\theta_i \\ &+\omega_E[\sin\theta_j\sin(\phi_i - \phi_j) + \sin\theta_k\sin(\phi_i - \phi_k)] \\ &+\omega_D[\sin\theta_j\cos(\phi_i - \phi_j) - \sin\theta_k\cos(\phi_i - \phi_k)] \\ &-\omega_A\sin\theta_i\sin[2(\phi_i - \Phi_i)] - \omega_T\sin\theta_i\big\},\end{aligned} \tag{A6}$$

where $\Phi_i = (i-1)3\pi/2$, and $\{i, j, k\} = \{1, 2, 3\}$, $\{2, 3, 1\}$, and $\{3, 1, 2\}$. By numerically integrating above 12-variable first-order differential equations, the evolutions of $\mathbf{m}_1$, $\mathbf{m}_2$, and $\mathbf{m}_3$ are plotted for the tilted AFM state, the FM state, and the self-oscillations in Fig. 5, corresponding to the parameter points a, b, c, d, e, and f marked in Fig. 2. In all these plots, the evolutions start from the ground state without the SOT, i.e., $\theta_1, \theta_2, \theta_3 = 0$, $\phi_1 = 0$, $\phi_2 = 2\pi/3$, and $\phi_3 = 4\pi/3$ initially. Besides, the initial angular velocities are set to zero ($\Omega_i^{\theta} = 0$, and $\Omega_i^{\phi} = 0$ initially).

APPENDIX B: STABILITY AND LINEAR OSCILLATION OF FERROMAGNETIC STATE

1. Secular equation

To analyze the stability of FM states, Eq. (6) is linearized in the vicinity of two FM equilibria, and assume $\mathbf{n} = \pm\mathbf{e}_z + n_x\mathbf{e}_x + n_y\mathbf{e}_y$, with n_x and n_y being the responses to a small perturbation. The general solutions for n_x and n_y are of the oscillating form $(n_x, n_y) = (\delta n_x, \delta n_y)e^{\lambda t}$ with $(\delta n_x, \delta n_y)$ being the amplitudes. Substituting this ansatz into Eq. (6) and retaining only the linear terms with respect to δn_x and δn_y, a linearized equation is obtained,

$$\begin{pmatrix}\lambda \pm \omega_T & f(\lambda) \\ -f(\lambda) + 3\omega_A & \lambda \pm \omega_T\end{pmatrix}\begin{pmatrix}\delta n_x \\ \delta n_y\end{pmatrix} = 0, \tag{B1}$$

where

$$f(\lambda) = \eta\lambda^2 + \alpha\lambda - 3\omega_E', \tag{B2}$$

with $\omega_E' = \omega_E - \sqrt{3}/3\omega_D$. To ensure a nontrivial solution, the determinant of the coefficient matrix must be zero. So, one gets the secular equation

$$a_0\lambda^4 + a_1\lambda^3 + a_2\lambda^2 + a_3\lambda + a_4 = 0, \tag{B3}$$

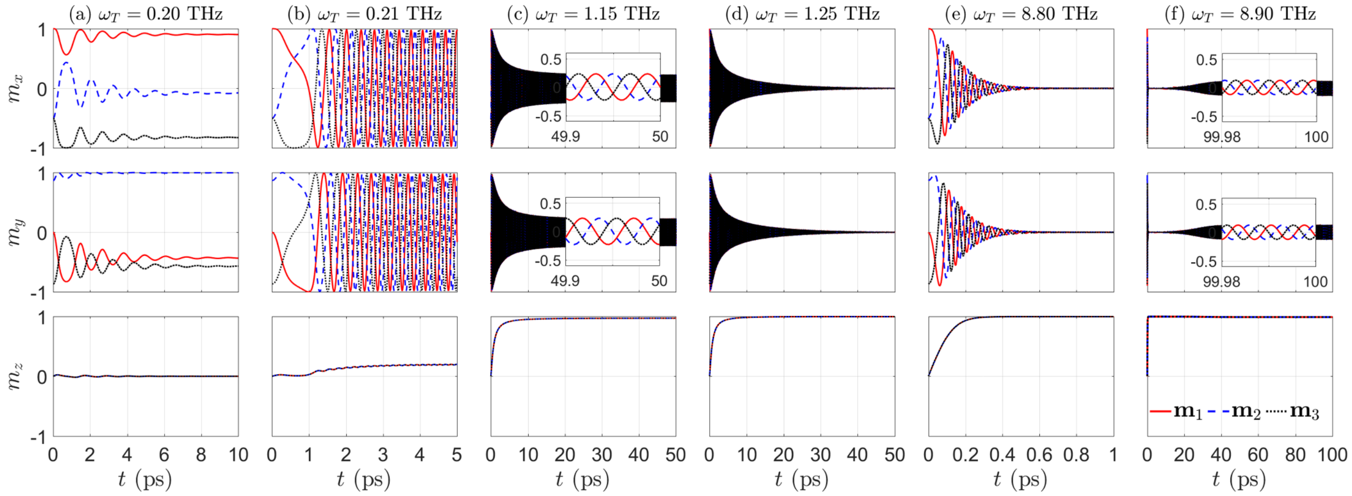

FIG. 5. Evolutions of $\mathbf{m}_1$, $\mathbf{m}_2$, and $\mathbf{m}_3$ for different states. The panels of first and second columns correspond to the tilted AFM state and the self-oscillation near the phase boundary defined by ω_T^l. The third and fourth columns correspond to the self-oscillation and the FM state near the boundary ω_T^-. The fifth and sixth columns correspond to the FM state and the self-oscillation near the boundary ω_T^+. The insets show magnified views of precessions. Six exemplary sets of parameters are picked up, as marked by the points a, b, c, d, e, and f in Fig. 2.

where

$$a_0 = \eta^2, \tag{B4}$$

$$a_1 = 2\alpha\eta, \tag{B5}$$

$$a_2 = 1 + \alpha^2 - 2\eta(3\omega_E' + \omega_A), \tag{B6}$$

$$a_3 = 2[\pm\omega_T - \alpha(3\omega_E' + \omega_A)], \tag{B7}$$

$$a_4 = \omega_T^2 + 3\omega_E'(3\omega_E' + 2\omega_A). \tag{B8}$$

2. Stability analysis

From the secular equation (B3), one can judge the stability of FM states without solving it. If the real parts of all λ are negative, perturbations decay in time, and the equilibrium is stable. This can be decided by the Routh-Hurwitz criterion [72–74]. Here, a series of determinants are defined:

$$\Delta_1 = a_1, \tag{B9}$$

$$\Delta_2 = \begin{vmatrix} a_1 & a_0 \\ a_3 & a_2 \end{vmatrix}, \tag{B10}$$

$$\Delta_3 = \begin{vmatrix} a_1 & a_0 & 0 \\ a_3 & a_2 & a_1 \\ 0 & a_4 & a_3 \end{vmatrix}, \tag{B11}$$

$$\Delta_4 = a_4\Delta_3. \tag{B12}$$

If all Δ are positive, the real parts of four roots of λ are negative. Then, the equilibrium state is stable. Inserting Eqs. (B5)–(B8) into Eqs. (B9)–(B12), the Routh-Hurwitz determinants are explicitly expressed as

$$\Delta_1 = 2\alpha\eta, \tag{B13}$$

$$\Delta_2 = 2\eta^2(\omega_T^c \mp \omega_T), \tag{B14}$$

$$\Delta_3 = 4(1 + \alpha^2)\eta^2(\omega_T^+ \mp \omega_T)(\omega_T \mp \omega_T^-), \tag{B15}$$

$$\Delta_4 = a_4\Delta_3, \tag{B16}$$

where

$$\omega_T^c = \frac{\alpha}{\eta}[1 + \alpha^2 - \eta(3\omega_E' + 2\omega_A)], \tag{B17}$$

and

$$\omega_T^\pm = \frac{\alpha}{2\eta}\left[1 \pm \sqrt{1 - 4\eta\left(3\omega_E' + \omega_A - \frac{\eta\omega_A^2}{1 + \alpha^2}\right)}\right]. \tag{B18}$$

It is evident that $\Delta_1 > 0$ and $a_4 > 0$ for any ω_T. Hence, one just need to judge the signs of Δ_2 and Δ_3. First, the condition of $\Delta_2 > 0$ is $|\omega_T| < \omega_T^c$. Second, solving $1 - 4\eta[3\omega_E' + \omega_A - \eta\omega_A^2/(1 + \alpha^2)] = 0$ yields

$$\eta_\pm = (1 + \alpha^2)\frac{3\omega_E' + \omega_A}{2\omega_A^2} \times \left[1 \pm \sqrt{1 - \frac{1}{1 + \alpha^2}\left(\frac{\omega_A}{3\omega_E' + \omega_A}\right)^2}\right]. \tag{B19}$$

If $\eta_- < \eta < \eta_+$, $\omega_T^\pm$ are complex conjugate. Thus, $\Delta_3 < 0$ for any ω_T, and the FM state is always unstable. On the other hand, if $\eta < \eta_-$ or $\eta > \eta_+$, $\Delta_3 > 0$ demands $\omega_T^- < |\omega_T| < \omega_T^+$.

For typical experimental parameters, $\omega_E \approx 10^{13}$ Hz, $\omega_A \approx 10^{11}$ Hz, and $\alpha \approx 0.01$, it can be estimated that $\eta_+ \approx 10^{-9}$ s, which is far beyond the range of inertial relaxation time (from fs to ps). So, only the critical value η_- is considered below. Under the premise of $\eta < \eta_-$, it can be proved that $\omega_T^c > \omega_T^+$. Thus, combining the conditions for $\Delta_2 > 0$ and $\Delta_3 > 0$, the FM state $\mathbf{m}_1, \mathbf{m}_2, \mathbf{m}_3 = \mathbf{e}_z$ is stable when $\eta < \eta_-$ and $\omega_T^- < \omega_T < \omega_T^+$, On the other hand, the FM state $\mathbf{m}_1, \mathbf{m}_2, \mathbf{m}_3 = -\mathbf{e}_z$ is stable when $\eta < \eta_-$ and $-\omega_T^+ < \omega_T < -\omega_T^-$.

3. Linear oscillations

To analyze the linear modes, $\lambda = -\chi + 2\pi i f$ is taken in the secular equation (B3), with χ being the attenuation factor and f the oscillating frequency. Even though Eq. (B3) can

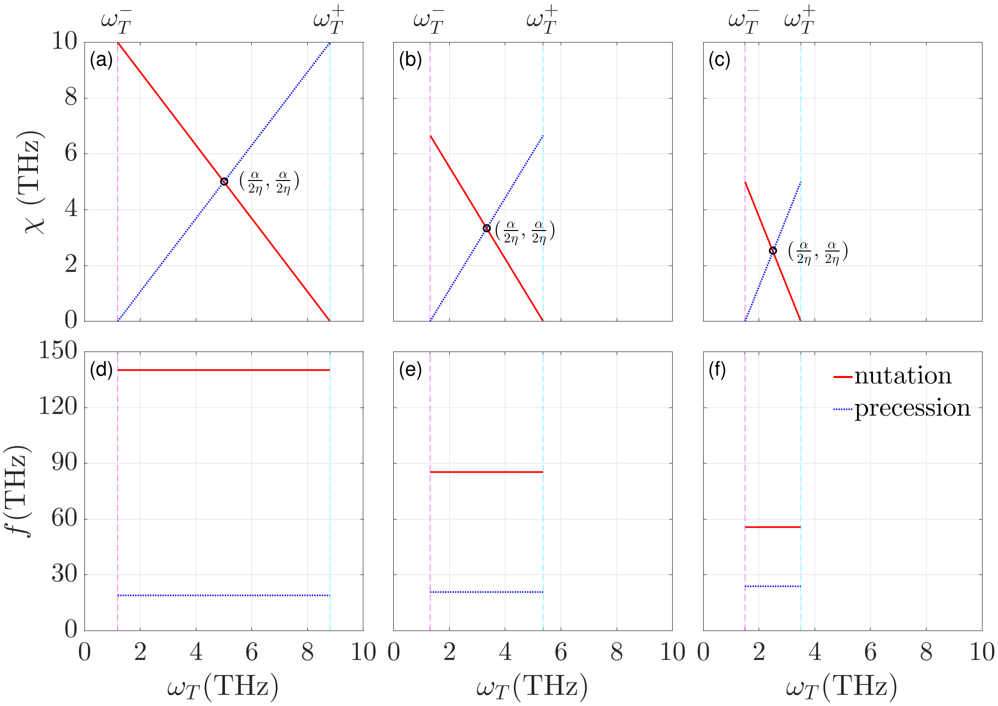

FIG. 6. The attenuation factor and the frequency of linear modes on top of the FM state as a function of the SOT strength ω_T. The lines are obtained by solving Eq. (B3). (a), (d) $\eta = 1$ ps. (b), (e) $\eta = 1.5$ ps. (c), (f) $\eta = 2$ ps.

be solved analytically, the expression is complicated. Then, after solving it numerically, the dependence of χ and f on ω_T is plotted in Fig. 6 for three η, corresponding to those in Fig. 3(a). It can be observed that the frequencies of both precession and nutation are almost independent of ω_T. In contrast, the attenuation factor of precession increases with ω_T, and that of nutation decreases with ω_T. Both lines of χ meet at a point defined by $(\omega_T, \chi) = (\alpha/(2\eta), \alpha/(2\eta))$. This can be obtained by assuming a set of roots $\lambda_1^{\pm} = -\chi \pm i\omega_1$ and $\lambda_2^{\pm} = -\chi \pm i\omega_2$, and equating the like orders of λ between Eq. (B3) and $(\lambda - \lambda_1^+)(\lambda - \lambda_1^-)(\lambda - \lambda_2^+)(\lambda - \lambda_2^-) = 0$. If $\omega_T < \omega_T^-$ ($\omega_T > \omega_T^+$), $\chi < 0$, meaning the divergence of the precession (nutation) mode. This is in line with the stable condition of FM states derived in Sec. B 2.

Setting $\alpha = 0$ and $\omega_T = 0$, the analytic solutions of Eq. (B3) is simple, which are just the eigenfrequencies of linear modes, i.e., Eq. (15) in the main text. $f_{FM}^{\pm}$ in Eq. (15) well reproduce the frequency curves in Figs. 6(d), 6(e), and 6(f).

APPENDIX C: STABILITY AND LINEAR OSCILLATION OF TILTED ANTIFERROMAGNETIC STATE

1. Secular equation

Besides the FM state, taking $d\mathbf{m}_i/dt = 0$ in Eq. (1) also yields four tilted AFM states, $\mathbf{m}_i = \cos(\phi_0 - \Phi_i)\mathbf{e}_x + \sin(\phi_0 - \Phi_i)\mathbf{e}_y$, where $\Phi_i = (i-1)3\pi/2$, and

$$\phi_0 = \frac{1}{2}\left[(P-1)\pi + (-1)^P \arcsin\frac{\omega_T}{\omega_A}\right], \tag{C1}$$

with $P = 1, 2, 3, 4$. These solutions reveal that the SOT rotates the in-plane configuration of $\mathbf{m}_i$ by an angle ϕ_0. $\mathbf{m}_1$, $\mathbf{m}_2$, and $\mathbf{m}_3$ still keep the 120° structure, leading to a compensation of exchange torques for each sublattice magnetization. The tilting from the easy axis allows the balance between the SOT and the anisotropy torque for every magnetization. In the effective formalism described by Eqs. (6)–(8), these tilted AFM states are expressed as $\mathbf{n} = \cos\phi_0\mathbf{e}_x + \sin\phi_0\mathbf{e}_y$.

To judge the stability of these equilibria, it is convenient to adopt the spherical coordinates of $\mathbf{n}$. Introducing the polar and azimuthal angles (θ, ϕ) as $\mathbf{n} = (\sin\theta\cos\phi, \sin\theta\sin\phi, \cos\theta)$, Eqs. (6)–(8) are transformed as

$$\begin{aligned}&\dot{\theta} + \alpha\sin\theta\dot{\phi} + \eta(2\cos\theta\dot{\theta}\dot{\phi} + \sin\theta\ddot{\phi})\\ &\quad = -(\omega_A\sin 2\phi + \omega_T)\sin\theta,\end{aligned} \tag{C2}$$

$$\begin{aligned}&\sin\theta\dot{\phi} - \alpha\dot{\theta} + \eta(\sin\theta\cos\theta\dot{\phi}^2 - \ddot{\theta})\\ &\quad = -(3\omega_E' + 2\omega_A\cos^2\phi)\sin\theta\cos\theta,\end{aligned} \tag{C3}$$

where the overdot indicates the derivative with respect to the time. Expressed by the spherical coordinates, the tilted AFM states are described by (θ_0, ϕ_0) with $\theta_0 = \pi/2$ and ϕ_0 being Eq. (C1).

According to the procedure of linear stability analysis, it can be assumed that $\theta = \theta_0 + \theta'$ and $\phi = \phi_0 + \phi'$ with θ' and ϕ' being the responses to a small perturbation and taking the oscillating form $(\theta', \phi') \propto e^{\lambda t}$. Inserting this ansatz into Eqs. (C2) and (C3), and keeping the linear terms of θ' and ϕ', one can obtain the linearized equations of the oscillating modes. To ensure a nontrivial solution, λ must obey the secular equation,

$$b_0\lambda^4 + b_1\lambda^3 + b_2\lambda^2 + b_3\lambda + b_4 = 0, \tag{C4}$$

where the coefficients are given as

$$b_0 = \eta^2, \tag{C5}$$

$$b_1 = 2\alpha\eta, \tag{C6}$$

$$b_2 = 1 + \alpha^2 + \eta[3\omega_E' + \omega_A - 3(-1)^P\tilde{\omega}_A], \tag{C7}$$

$$b_3 = \alpha(3\omega_E' + \omega_A - 3(-1)^P\tilde{\omega}_A), \tag{C8}$$

$$b_4 = 2[-(-1)^P(3\omega_E' + \omega_A) + \tilde{\omega}_A]\tilde{\omega}_A, \tag{C9}$$

with $\tilde{\omega}_A = (\omega_A^2 - \omega_T^2)^{1/2}$.

2. Stability analysis

By the same procedure as Sec. B 2, the corresponding Routh-Hurwitz determinants are obtained

$$\Delta_1 = 2\alpha\eta, \tag{C10}$$

$$\Delta_2 = 2\alpha\eta(1 + \alpha^2) + \alpha\eta^2[3\omega_E' + \omega_A - 3(-1)^P\tilde{\omega}_A], \tag{C11}$$

$$\begin{aligned}\Delta_3 = {} & 2\alpha^2(1 + \alpha^2)\eta[3\omega_E' + \omega_A - 3(-1)^P\tilde{\omega}_A] \\ & + \alpha^2\eta^2[3\omega_E' + \omega_A + (-1)^P\tilde{\omega}_A]^2,\end{aligned} \tag{C12}$$

$$\Delta_4 = a_4\Delta_3. \tag{C13}$$

Definitely, $\Delta_1 > 0$. In view of $\omega_E \gg \omega_A$, Δ_2 and Δ_3 are positive for $P = 1, 2, 3, 4$. From Eq. (C9), it is easy to infer that $a_4 > 0$ for $P = 1, 3$, meanwhile $a_4 < 0$ for $P = 2, 4$. Furthermore, from Eq. (C13), one has $\Delta_4 > 0$ for $P = 1, 3$, and $\Delta_4 < 0$ for $P = 2, 4$. Therefore, for $P = 1, 3$, all Δ are positive, and the corresponding solutions are stable. It must be noted that the tilted AFM solutions exist only for $|\omega_T| \leqslant \omega_A$, as observed from Eq. (C1).

3. Frequencies of linear oscillations

Except when used for stability analysis, the secular equation (C4) can also be directly solved by assuming $\lambda = -\chi + 2\pi i f$, with χ being the attenuation factor and f the oscillating frequency. For a complex quartic equation, the analytic roots of χ and f are too complicated. However, after neglecting α, one can get the eigenfrequencies approximately, i.e., Eq. (14) in the main text. As comparing with numeric results in the insets of Figs. 3(a) and 3(c), the approximate analytic results largely capture the feature of dispersion.

APPENDIX D: LOWER THRESHOLD OF SELF-OSCILLATION

From Sec. C 2, the tilted AFM states exist and are linearly stable for a weak SOT ($\omega_T \leqslant \omega_A$). Nevertheless, this instability boundary does not agree with the numeric result [see Figs. 5(a) and 5(b)]. Next, this boundary will be defined by applying the averaging technique on the self-oscillation near its lower threshold.

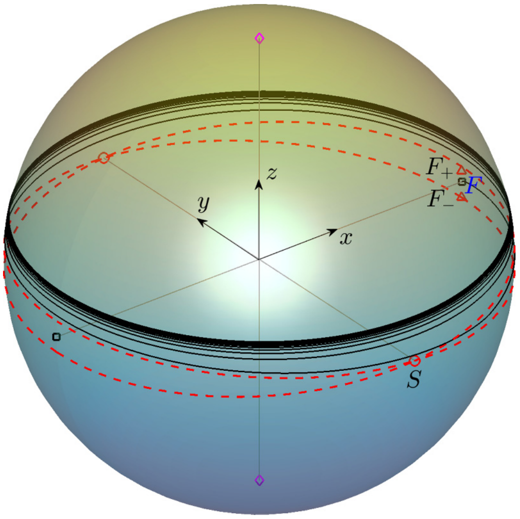

FIG. 7. Trajectory (solid curves) of **n** near the lower threshold of self-oscillation with $\omega_T = 0.21$ THz, corresponding to the evolutions of $\mathbf{m}_1$, $\mathbf{m}_2$, and $\mathbf{m}_3$ in Fig. 5(b). The dashed curves are the separatrices corresponding to $\mathcal{E}_n = \mathcal{E}_{\text{saddle}}$.

The analytic calculations are carried out by use of the reduced equation [Eq. (6)], which represents the magnetic dynamics of the three sublattices and is analytically tractable. In view of the energetics of **n**, three kinds of fixed points are defined: two minima with $\mathbf{n} = \pm\mathbf{e}_x$ and $\mathcal{E}_{min} = -\omega_A$, two maxima with $\mathbf{n} = \pm\mathbf{e}_z$ and $\mathcal{E}_{max} = 3/2\omega_E'$, as well as two saddles with $\mathbf{n} = \pm\mathbf{e}_y$ and $\mathcal{E}_{\text{saddle}} = 0$. As argued in Refs. [7,8,10], the equal-energy trajectories are classified into two kinds: the low-energy trajectories signified by $\mathcal{E}_{min} < \mathcal{E}_n < \mathcal{E}_{\text{saddle}}$, and the high-energy ones $\mathcal{E}_{\text{saddle}} < \mathcal{E}_n < \mathcal{E}_{max}$. In addition, there exist two separatrices (dashed curves in Figs. 7) at $\mathcal{E}_n = \mathcal{E}_{\text{saddle}}$, dividing the low-energy and high-energy regions on the spherical surface [8,10]. These two separatrices connect the two saddles. By inserting $\mathcal{E}_n = \mathcal{E}_{\text{saddle}} = 0$ into Eq. (7), and combining with the constraint $n_x^2 + n_y^2 + n_z^2 = 1$, the separatrices are parametrized as

$$n_x = \sqrt{\frac{3\omega_E}{3\omega_E + 2\omega_A}}\cos\xi, \tag{D1}$$

$$n_y = \sin\xi, \tag{D2}$$

with ξ changing from 0 to 2π.

Considering the balance between the damping-like SOT and the damping torque, it is possible to sustain a stable self-oscillation only on the high-energy trajectories, which are around $\pm\mathbf{e}_z$, not $\pm\mathbf{e}_x$. Therefore, there exists an energy barrier ($\mathcal{E}_{\text{saddle}} - \mathcal{E}_{min} = \omega_A$) between the initial state ($\mathbf{n} = \mathbf{e}_x$ or $-\mathbf{e}_x$) and the self-oscillation trajectory with the lowest energy. When **n** evolves from the initial direction (exemplified by the point F in Fig. 7) to the self-oscillation near the saddle (the point S), the SOT not only counteracts the damping but also pushes **n** across the barrier. This results in a work-energy relation

$$\omega_T \int_F^S (\mathbf{n} \times \mathbf{e}_z) \cdot d\mathbf{n} = \alpha \int_F^S \left(\mathbf{n} \times \frac{d\mathcal{E}_n}{d\mathbf{n}}\right) \cdot d\mathbf{n} + \omega_A. \tag{D3}$$

Given that there is no analytic formula to describe the trajectory from F to S, the integrals above cannot be performed analytically. Nevertheless, due to the strong exchange ($\omega_E \gg \omega_A$), it can be inferred from Eqs. (D1) and (D2) that the separatrices are very close to the evolution trajectory from F to S (see the dashed lines in Fig. 7). Namely, the points $F_{\pm}$ (intersections between the separatrices and the z-x plane) are near F. Therefore, the integrals in Eq. (D3) can be well approximated by those along the trajectory from F_+ (or F_-) to S. Utilizing Eqs. (D1) and (D2), as well as $n_z = (n_x^2 + n_y^2)^{1/2}$, the variable of integration becomes ξ varying from 0 to $\pi/2$. Performing the integrals, and retaining the first-order terms with respect to α and ω_T, one arrives at Eq. (13) in the main text from Eq. (D3).

[1] R. Cheng, M. W. Daniels, J.-G. Zhu, and D. Xiao, Ultrafast switching of antiferromagnets via spin-transfer torque, Phys. Rev. B **91**, 064423 (2015).

[2] R. Cheng, D. Xiao, and A. Brataas, Terahertz antiferromagnetic spin Hall nano-oscillator, Phys. Rev. Lett. **116**, 207603 (2016).

[3] O. R. Sulymenko, O. V. Prokopenko, V. S. Tiberkevich, A. N. Slavin, B. A. Ivanov, and R. S. Khymyn, Terahertz-frequency spin Hall auto-oscillator based on a canted antiferromagnet, Phys. Rev. Appl. **8**, 064007 (2017).

[4] R. Khymyn, I. Lisenkov, V. Tiberkevich, B. A. Ivanov, and A. Slavin, Antiferromagnetic THz-frequency Josephson-like oscillator driven by spin current, Sci. Rep. **7**, 43705 (2017).

[5] V. Puliafito, R. Khymyn, M. Carpentieri, B. Azzerboni, V. Tiberkevich, A. Slavin, and G. Finocchio, Micromagnetic modeling of terahertz oscillations in an antiferromagnetic material driven by the spin Hall effect, Phys. Rev. B **99**, 024405 (2019).

[6] D.-K. Lee, B.-G. Park, and K.-J. Lee, Antiferromagnetic oscillators driven by spin currents with arbitrary spin polarization directions, Phys. Rev. Appl. **11**, 054048 (2019).

[7] Q.-H. Li, P.-B. He, M.-Q. Cai, and Z.-D. Li, Equilibria and precession in a uniaxial antiferromagnet driven by the spin Hall effect, New J. Phys. **23**, 113020 (2021).

[8] Y.-Q. Zhao, P.-B. He, and M.-Q. Cai, Tunable range of terahertz oscillations triggered by the spin Hall effect in a biaxial antiferromagnet, Phys. Rev. B **106**, 134427 (2022).

[9] P.-B. He, Large-amplitude and widely tunable self-oscillations enabled by the inertial effect in uniaxial antiferromagnets driven by spin-orbit torques, Phys. Rev. B **108**, 184418 (2023).

[10] D.-Y. Zhao, P.-B. He, and M.-Q. Cai, Terahertz oscillation in a noncollinear antiferromagnet under spin-orbit torques, Phys. Rev. B **104**, 214423 (2021).

[11] A. Shukla and S. Rakheja, Spin-torque-driven terahertz auto-oscillations in noncollinear coplanar antiferromagnets, Phys. Rev. Appl. **17**, 034037 (2022).

[12] M. A. Lund, D. R. Rodrigues, K. Everschor-Sitte, and K. M. D. Hals, Voltage-controlled high-bandwidth terahertz oscillators based on antiferromagnets, Phys. Rev. Lett. **131**, 156704 (2023).

[13] S. Hu, C. Zheng, C. Chen, Y. Zhou, and Y. Liu, Current-driven spin oscillations in noncollinear antiferromagnetic tunnel junctions, Phys. Rev. B **109**, 174433 (2024).

[14] H. Chen, Q. Niu, and A. H. MacDonald, Anomalous Hall effect arising from noncollinear antiferromagnetism, Phys. Rev. Lett. **112**, 017205 (2014).

[15] O. V. Gomonay and V. M. Loktev, Using generalized Landau-Lifshitz equations to describe the dynamics of multi-sublattice antiferromagnets induced by spin-polarized current, Low Temp. Phys. **41**, 698 (2015).

[16] H. Fujita, Field-free, spin-current control of magnetization in non-collinear chiral antiferromagnets, Phys. Status Solidi RRL **11**, 1600360 (2017).

[17] T. Hajiri, S. Ishino, K. Matsuura, and H. Asano, Electrical current switching of the noncollinear antiferromagnet Mn_3GaN, Appl. Phys. Lett. **115**, 052403 (2019).

[18] G. Gurung, D.-F. Shao, and E. Y. Tsymbal, Spin-torque switching of noncollinear antiferromagnetic antiperovskites, Phys. Rev. B **101**, 140405(R) (2020).

[19] R. Mondal, L. Rózsa, M. Farle, P. M. Oppeneer, U. Nowak, and M. Cherkasskii, Inertial effects in ultrafast spin dynamics, J. Magn. Magn. Mater. **579**, 170830 (2023).

[20] T. L. Gilbert, A phenomenological theory of damping in ferromagnetic materials, IEEE Trans. Magn. **40**, 3443 (2004).

[21] J.-E. Wegrowe and M.-C. Ciornei, Magnetization dynamics, gyromagnetic relation, and inertial effects, Am. J. Phys. **80**, 607 (2012).

[22] S. Giordano and P.-M. Déjardin, Magnetization dynamics, gyromagnetic relation, and inertial effects, Phys. Rev. B **102**, 214406 (2020).

[23] M.-C. Ciornei, J. M. Rubí, and J.-E. Wegrowe, Magnetization dynamics in the inertial regime: Nutation predicted at short time scales, Phys. Rev. B **83**, 020410(R) (2011).

[24] M. Fähnle, D. Steiauf, and C. Illg, Generalized Gilbert equation including inertial damping: Derivation from an extended breathing Fermi surface model, Phys. Rev. B **84**, 172403 (2011).

[25] M. Fähnle and C. Illg, Electron theory of fast and ultrafast dissipative magnetization dynamics, J. Phys.: Condens. Matter **23**, 493201 (2011).

[26] R. Mondal, M. Berritta, A. K. Nandy, and P. M. Oppeneer, Relativistic theory of magnetic inertia in ultrafast spin dynamics, Phys. Rev. B **96**, 024425 (2017).

[27] R. Mondal, M. Berritta, and P. M. Oppeneer, Generalisation of Gilbert damping and magnetic inertia parameter as a series of higher-order relativistic terms, J. Phys.: Condens. Matter **30**, 265801 (2018).

[28] U. Bajpai and B. K. Nikolić, Time-retarded damping and magnetic inertia in the Landau-Lifshitz-Gilbert equation self-consistently coupled to electronic time-dependent nonequilibrium Green functions, Phys. Rev. B **99**, 134409 (2019).

[29] S. Bhattacharjee, L. Nordström, and J. Fransson, Atomistic spin dynamic method with both damping and moment of inertia effects included from first principles, Phys. Rev. Lett. **108**, 057204 (2012).

[30] P. Thibaudeau and S. Nicolis, Emerging magnetic nutation, Eur. Phys. J. B **94**, 196 (2021).

[31] F. Xu, G. Li, J. Chen, Z. Yu, L. Zhang, B. Wang, and J. Wang, Unified framework of the microscopic Landau-Lifshitz-Gilbert equation and its application to skyrmion dynamics, Phys. Rev. B **108**, 144409 (2023).

[32] Y. Li, A.-L. Barra, S. Auffret, U. Ebels, and W. E. Bailey, Inertial terms to magnetization dynamics in ferromagnetic thin films, Phys. Rev. B **92**, 140413(R) (2015).

[33] K. Neeraj, N. Awari, S. Kovalev, D. Polley, N. Z. Hagström, S. S. P. K. Arekapudi, A. Semisalova, K. Lenz, B. Green, J.-C. Deinert, I. Ilyakov, M. Chen, M. Bawatna, V. Scalera, M. d'Aquino, C. Serpico, O. Hellwig, J.-E. Wegrowe, M. Gensch, and S. Bonetti, Inertial spin dynamics in ferromagnets, Nat. Phys. **17**, 245 (2021).

[34] V. Unikandanunni, R. Medapalli, M. Asa, E. Albisetti, D. Petti, R. Bertacco, E. E. Fullerton, and S. Bonetti, Inertial spin dynamics in epitaxial cobalt films, Phys. Rev. Lett. **129**, 237201 (2022).

[35] E. Olive, Y. Lansac, and J.-E. Wegrowe, Beyond ferromagnetic resonance: The inertial regime of the magnetization, Appl. Phys. Lett. **100**, 192407 (2012).

[36] D. Böttcher and J. Henk, Significance of nutation in magnetization dynamics of nanostructures, Phys. Rev. B **86**, 020404(R) (2012).

[37] E. Olive, Y. Lansac, M. Meyer, M. Hayoun, and J.-E. Wegrowe, Deviation from the Landau-Lifshitz-Gilbert equation in the inertial regime of the magnetization, J. Appl. Phys. **117**, 213904 (2015).

[38] M. Cherkasskii, M. Farle, and A. Semisalova, Deterministic inertial dynamics of the magnetization of nanoscale ferromagnets, Phys. Rev. B **102**, 184432 (2020).

[39] R. Mondal, Theroy of magnetic inertial dynamics in two-sublattice ferromagnets, J. Phys.: Condens. Matter **33**, 275804 (2021).

[40] S. V. Titov, W. T. Coffey, Y. P. Kalmykov, and M. Zarifakis, Deterministic inertial dynamics of the magnetization of nanoscale ferromagnets, Phys. Rev. B **103**, 214444 (2021).

[41] M. Cherkasskii, I. Barsukov, R. Mondal, M. Farle, and A. Semisalova, Theory of inertial spin dynamics in anisotropic ferromagnets, Phys. Rev. B **106**, 054428 (2022).

[42] S. V. Titov, W. J. Dowling, and Y. P. Kalmykov, Ferromagnetic and nutation resonance frequencies of nanomagnets with various magnetocrystalline anisotropies, J. Appl. Phys. **131**, 193901 (2022).

[43] R. Mondal, S. Großenbach, L. Rózsa, and U. Nowak, Nutation in antiferromagnetic resonance, Phys. Rev. B **103**, 104404 (2021).

[44] R. Mondal and P. M. Oppeneer, Influence of intersublattice coupling on the terahertz nutation spin dynamics in antiferromagnets, Phys. Rev. B **104**, 104405 (2021).

[45] R. Mondal and A. Kamra, Spin pumping at terahertz nutation resonances, Phys. Rev. B **104**, 214426 (2021).

[46] R. Rodriguez, M. Cherkasskii, R. Jiang, R. Mondal, A. Etesamirad, A. Tossounian, B. A. Ivanov, and I. Barsukov, Spin inertia and auto-oscillations in ferromagnets, Phys. Rev. Lett. **132**, 246701 (2024).

[47] I. Makhfudz, E. Olive, and S. Nicolis, Nutation wave as a platform for ultrafast spin dynamics in ferromagnets, Appl. Phys. Lett. **117**, 132403 (2020).

[48] M. Cherkasskii, M. Farle, and A. Semisalova, Dispersion relation of nutation surface spin waves in ferromagnets, Phys. Rev. B **103**, 174435 (2021).

[49] A. M. Lomonosov, V. V. Temnov, and J.-E. Wegrowe, Nutation spin waves in ferromagnets, Phys. Rev. B **104**, 054425 (2021).

[50] S. V. Titov, W. J. Dowling, Y. P. Kalmykov, and M. Cherkasskii, Nutation spin waves in ferromagnets, Phys. Rev. B **105**, 214414 (2022).

[51] R. Mondal and L. Rózsa, Inertial spin waves in ferromagnets and antiferromagnets, Phys. Rev. B **106**, 134422 (2022).

[52] M. Cherkasskii, R. Mondal, and L. Rózsa, Inertial spin waves in spin spirals, Phys. Rev. B **109**, 184424 (2024).

[53] R. Rahman and S. Bandyopadhyay, An observable effect of spin inertia in slow magneto-dynamics: Increase of the switching error rates in nanoscale ferromagnets, J. Phys.: Condens. Matter **33**, 355801 (2021).

[54] K. Neeraj, M. Pancaldi, V. Scalera, S. Perna, M. d'Aquino, C. Serpico, and S. Bonetti, Magnetization switching in the inertial regime, Phys. Rev. B **105**, 054415 (2022).

[55] I. Makhfudz, Y. Hajati, and E. Olive, High-temperature magnetization reversal in the inertial regime, Phys. Rev. B **106**, 134415 (2022).

[56] L. Winter, S. Großenbach, U. Nowak, and L. Rózsa, Nutational switching in ferromagnets and antiferromagnets, Phys. Rev. B **106**, 214403 (2022).

[57] J. Liu and L. Balents, Anomalous Hall effect and topological defects in antiferromagnetic Weyl semimetals: Mn_3Sn/Ge, Phys. Rev. Lett. **119**, 087202 (2017).

[58] M. Mochizuki, M. Kobayashi, R. Okabe, and D. Yamamoto, Spin model for nontrivial types of magnetic order in inverse-perovskite antiferromagnets, Phys. Rev. B **97**, 060401(R) (2018).

[59] J.-R. Soh, F. de Juan, N. Qureshi, H. Jacobsen, H.-Y. Wang, Y.-F. Guo, and A. T. Boothroyd, Ground-state magnetic structure of Mn_3Ge, Phys. Rev. B **101**, 140411(R) (2020).

[60] H. Tsai, T. Higo, K. Kondou, T. Nomoto, A. Sakai, A. Kobayashi, T. Nakano, K. Yakushiji, R. Arita, S. Miwa, Y. Otani, and S. Nakatsuji, Electrical manipulation of a topological antiferromagnetic state, Nature (London) **580**, 608 (2020).

[61] Y. Takeuchi, Y. Yamane, J.-Y. Yoon, R. Itoh, B. Jinnai, S. Kanai, J. Ieda, S. Fukami, and H. Ohno, Chiral-spin rotation of non-collinear antiferromagnet by spin-orbit torque, Nat. Mater. **20**, 1364 (2021).

[62] A. Manchon, J. Železný, I. M. Miron, T. Jungwirth, J. Sinova, A. Thiaville, K. Garello, and P. Gambardella, Current-induced spin-orbit torques in ferromagnetic and antiferromagnetic systems, Rev. Mod. Phys. **91**, 035004 (2019).

[63] D. Thonig, O. Eriksson, and M. Pereiro, Magnetic moment of inertia within the torque-torque correlation model, Sci. Rep. **7**, 931 (2017).

[64] L. Zhu, D. C. Ralph, and R. A. Buhrman, Highly efficient spin-current generation by the spin Hall effect in $Au_{1-x}Pt_x$, Phys. Rev. Appl. **10**, 031001(R) (2018).

[65] C. F. Pai, Y. Ou, L. H. Vilela-Leão, D. C. Ralph, and R. A. Buhrman, Dependence of the efficiency of spin Hall torque on the transparency of Pt/ferromagnetic layer interfaces, Phys. Rev. B **92**, 064426 (2015).

[66] Z. L. Wang, H. Y. Cheng, K. W. Shi, Y. Liu, J. F. Qiao, D. Q. Zhu, W. L. Cai, X. Y. Zhang, S. Eimer, D. P. Zhu, J. Zhang, A. Fert, and W. S. Zhao, Modulation of field-like spin orbit torque in heavy metal/ferromagnet heterostructures, Nanoscale **12**, 15246 (2020).

[67] G. Bertotti, C. Serpico, I. D. Mayergoyz, A. Magni, M. dAquino, and R. Bonin, Magnetization switching and microwave oscillations in nanomagnets driven by spin-polarized currents, Phys. Rev. Lett. **94**, 127206 (2005).

[68] G. Bertotti, I. D. Mayergoyz, and C. Serpico, *Nonlinear Magnetization Dynamics in Nanosystems* (Elsevier, Oxford, UK, 2009), pp. 100–105, 242–260.

[69] A. Thiaville and Y. Nakatani, *Spin Dynamics in Confined Magnetic Structures III*, edited by B. Hillebrands and A. Thiaville (Springer, New York, 2006), pp. 269–274, 295–300.

[70] T. Taniguchi and H. Kubota, Instability analysis of spin-torque oscillator with an in-plane magnetized free layer and a perpendicularly magnetized pinned layer, Phys. Rev. B **93**, 174401 (2016).

[71] S. Tomiyoshi and Y. Yamaguchi, Magnetic structure and weak ferromagnetism of Mn_3Sn studied by polarized neutron diffraction, J. Phys. Soc. Jpn. **51**, 2478 (1982).

[72] F. R. Gantmacher, *Applications of the Theory of Matrices* (Wiley, New York, 1959), p. 231.

[73] L. J. S. Allen, *An Introduction to Mathematical Biology* (Pearson Education Inc., 2007), p. 150.

[74] P. Baláž and J. Barnaś, Current-induced instability of a composite free layer with antiferromagnetic interlayer coupling, Phys. Rev. B **88**, 014406 (2013).